Macromolecules
Cite This: Macromolecules XXXX, XXX, XXX–XXX
Article
pubs.acs.org/Macromolecules

Comparing Morphological Evolution during Tensile Deformation of Two Precise Polyethylenes via 2D Fitting of *in Situ* X-ray Scattering

Edward B. Trigg,[†] L. Robert Middleton,[†] Lu Yan,[‡] and Karen I. Winey*[,†,‡]

[†]Department of Materials Science and Engineering and [‡]Department of Chemical and Biomolecular Engineering, University of Pennsylvania, Philadelphia, Pennsylvania 19104, United States

Supporting Information

ABSTRACT: Some types of precise polyethylenes, or linear polyethylenes containing precisely periodic functional groups, exhibit significant strain hardening under tensile deformation. Here we perform *in situ* X-ray scattering during tensile deformation of two precise polyethylenes: one with pendant carboxylic acid groups every 21st carbon (p21AA) and another with pendant imidazolium bromide groups every 15th carbon (p15ImBr). p21AA exhibits significant strain hardening and its layered structure orients with the layer normal along the tensile axis, while p15ImBr does *not* exhibit strain hardening and its layer normal orients *perpendicular* to the tensile axis. Quantitative evaluation of the 2D fiber patterns shows that p21AA undergoes a morphological transition, from a semicrystalline structure to a nanofibrillar structure, while the morphology of p15ImBr reorients and the chain folding structure is preserved. This suggests that fibrillization plays an important role in the strain hardening mechanism.

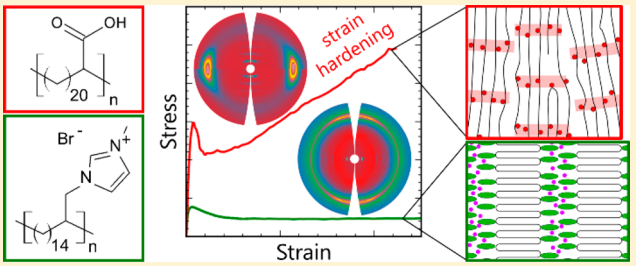

INTRODUCTION

The addition of side groups to semicrystalline polymers has a significant impact on morphology, crystallinity, and mechanical properties. The commercially important polymers Nucrel (DuPont) and Escor (Dow) are random copolymers of ethylene and methacrylic acid with their compositions tuned to achieve targeted mechanical, adhesive, and optical properties. Their carboxylic acids hydrogen bond, acting as reversible cross-links to improve mechanical strength and reducing the crystallinity of the polymer.

Sequence control in polymers can enable engineering of polymer conformations and morphologies, thereby producing previously inaccessible properties.[1−3] In particular, precisely periodic placement of interacting groups along linear polyethylene has attracted considerable interest.[4−9] Recently, it was shown that a linear polyethylene containing precisely periodic pendant carboxylic acid groups on every 21st carbon (Figure 1a) exhibits an unusual crystal motif wherein multiple layers of hairpin-folded chains exist within a single crystalline domain,[10,11] similar to some grafted long-spaced polyesters.[12,13] Middleton et al. showed that layers of hydrogen-bonded acid groups in this precise polymer orient with their normal vectors parallel to the deformation and reinforce the material, causing increased strain hardening relative to the random copolymer.[14,15] This strain-hardening mechanism also occurs in similar precise polyethylenes containing phosphonic acid and geminal carboxylic acid, but not in polyethylene with pseudorandomly placed acid groups.[16] The morphological evolutions in these polymers were observed via *in situ* X-ray scattering.

A wealth of quantitative structural information can be extracted from X-ray scattering patterns of materials with fiber symmetry by fitting the two-dimensional scattering patterns. In 2010, Burger et al. presented a thorough review of quantitative modeling of fiber scattering patterns.[17] In most cases, a Bragg peak arising from a single structural unit in the material can be modeled with a Gaussian or Lorentzian shape in both the radial and tangential directions. Nonuniform preferential orientation of an ensemble of such structural units in a material leads to a peak shape that is neither an arc nor a spot but somewhere in between.

At high tensile strains, precise acid-containing polyethylenes such as the one shown in Figure 1a exhibit preferential orientation of the chains along the tensile axis, as do most polymers under tensile deformation, and also show alignment of the acid layer normal vectors along tensile axis. This is readily seen from the equatorial orientation of the 100_{hex} peak and the meridional orientation of the layer peaks (Figure 1b). Surprisingly, Buitrago et al. reported via *ex situ* X-ray scattering that two precise polyethylenes containing imidazolium bromide side groups—one every 15th carbon (Figure 1c) and the other every 21st carbon—oriented in the opposite manner.[18] In both imidazolium bromide polymers, at high strains the chains are oriented *perpendicular* to the tensile axis, as are the layer normal vectors (Figure 1d). Here, we investigate in detail the morphological changes during tensile deformation of the

Received: July 31, 2018
Revised: September 20, 2018

Downloaded from pubs.acs.org by UNIV OF LOUISIANA AT LAFAYETTE on 10/03/18. For personal use only.

© XXXX American Chemical Society

DOI: 10.1021/acs.macromol.8b01639
Macromolecules XXXX, XXX, XXX–XXX

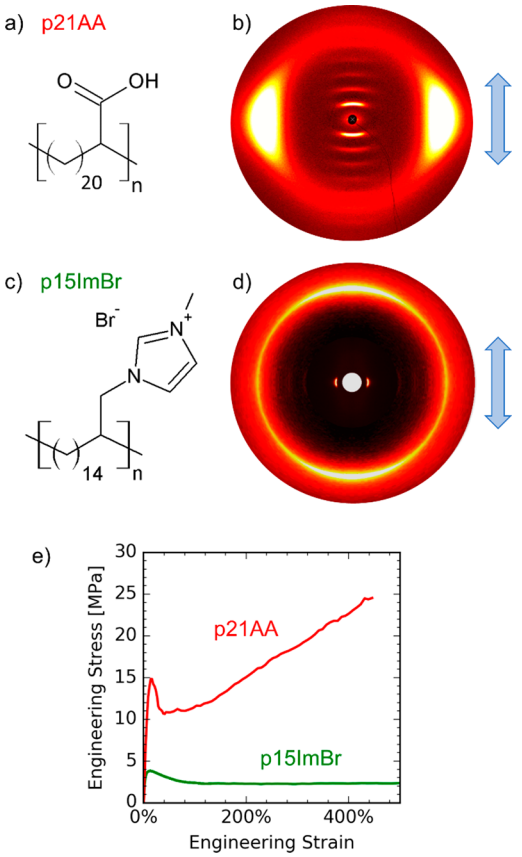

Figure 1. (a) Chemical structure of p21AA and (b) X-ray scattering of p21AA at high strain (ε = 500%), adopted from Middleton et al.[14] (c) Chemical structure of p15ImBr and (d) X-ray scattering of p15ImBr at high strain (ε = 400%). Blue arrows indicate the tensile axis in (b) and (d). (e) Engineering stress−strain curves for p21AA[14] and p15ImBr under *ex situ* uniaxial tensile deformation. p21AA exhibits significantly more strain hardening after yield. The strain rate is 1.77 s^{-1} at room temperature.

precise polyethylene with carboxylic acid groups every 21st carbon (termed p21AA)[19] and the precise polyethylene with imidazolium bromide groups every 15th carbon (termed p15ImBr).[20] Two key differences in these materials are already apparent from Figure 1: the opposing orientations of the layered structures in the two polymers and the significantly higher yield strength and strain hardening in p21AA (Figure 1e). With a new computer code[21] based on the mathematics presented by Burger et al.,[17] we reveal morphological features by quantitatively fitting the *in situ* X-ray scattering in 2D as a function of strain. This 2D fitting of *in situ* X-ray scattering has not been reported previously for precise polyethylenes. The fitting results suggest the underlying causes of the differences in morphology and mechanical behavior.

METHODS

Materials. The synthetic batches of p21AA and p15ImBr used for this study were reported previously.[14,20] Previous gel permeation chromatography (GPC) and differential scanning calorimetry (DSC) results are summarized in Table 1. All samples are stored at room temperature under vacuum.

***Ex Situ* Tensile Test.** An *ex situ* uniaxial tensile test of p15ImBr (shown in Figure 1e) was performed on an Instron 5564 table mounted materials testing system. Samples were hot pressed above the melting temperature, cooled at ∼15 °C/min, and cut into dogbone shapes with gauge length 10 mm, gauge width 5 mm, and gauge thickness 0.13 mm. Samples were aged at least 3 days in an evacuated desiccator before tensile tests. The strain rate was 1.77 s^{-1}.

Table 1. GPC, DSC, and TGA Characterization of p21AA and p15ImBr

polymer	M_n[a] [kg/mol]	dispersity (M_w/M_n)[a]	melting temp[b] [°C]	water content[c] [wt %]	water content [n_{H_2O}/n_{FG}][c,d]
p21AA	18.3[14]	1.9[14]	46[14]	0.7	0.1
p15ImBr	44.0[20]	2.0[20]	49, 70[18]	3.5	0.8

[a]From GPC. [b]From DSC, 10 °C/min heating ramp. [c]From TGA (see Figure S2). [d]Moles of water per mole of functional group (i.e., carboxylic acid or imidazolium bromide).

Thermogravimetric Analysis (TGA). TGA was performed on both polymers using a Sdt Q600 (TA Instruments) with flowing nitrogen gas (100 mL/min). Sample masses were 11.7 mg for p21AA and 12.8 mg for p15ImBr. Samples were exposed to ambient air (∼21 °C and ∼40% relative humidity) for at least 2 h before the experiments were run. The temperature profiles for the TGA run were as follows: a constant temperature of 25 °C for 2 min, then a ramp from 25 to 150 °C at a rate of 5 °C/min, followed by a constant temperature of 150 °C for 120 min (see Figure S2).

***In Situ* X-ray Scattering.** Samples of p21AA and p15ImBr were hot pressed above the melting temperature (T_m) to a thickness of 0.13 mm, cooled at ∼15 °C/min, aged at least 3 days under vacuum, and cut into dogbone or bowtie shapes. *In situ* tensile testing was performed at the Advanced Photon Source, part of Argonne National Laboratory, at beamline 5ID-D (DND-CAT). The tensile stage and X-ray source (λ = 0.73 Å) and detector setup were described previously.[14,16] X-ray scattering patterns had a collection time of 1 s, and the time between collections (refresh time) was 6 s for p21AA and 3.5 s for p15ImBr. For p21AA, a single detector was used with a sample-to-detector distance of 32 cm, while for p15ImBr, three detectors were used with sample-to-detector distances of 14, 20, and 800 cm. An additional *in situ* tensile test was performed on p21AA with a sample-to-detector distance of 800 cm to observe the small-angle X-ray scattering shown in Figure S1a.

Fitting X-ray Scattering of p15ImBr. Unlike those of p21AA, the layer peaks of p15ImBr were circles or arcs centered on the main beam, indicating no noticeable tangential width. Thus, the layer peaks of p15ImBr did not require 2D fitting like p21AA. The layer peak position and width were tracked as a function of strain by fitting 1D I vs q plots integrated over all azimuthal angles with a simple Lorentzian function and a linear background. The layer peak intensity distribution (Figure 6) was tracked at each scattering image by generating I vs q plots of 2° wedges, fitting and subtracting a linear background, and then integrating the remaining intensity over a q range corresponding to the peak.

Fitting X-ray Scattering of p21AA. During deformation, the layer peaks of p21AA had a shape that was not an arc centered at the primary beam, nor was it a spot, but somewhere in between. Therefore, we fit this peak using the equations provided by Burger et al.,[17,22] namely

$$J(q, \phi) = \int_0^{\pi/2} I(q, \phi')F(\phi, \phi') \sin \phi' \, d\phi' \quad (1)$$

where J is the scattering intensity at a point in reciprocal space defined by distance q from the origin and angle ϕ from the fiber axis. $I(q,\phi')$ is the scattering from a single scatterer at an angle ϕ' from the reciprocal lattice vector. $F(\phi,\phi')$ is the integration kernel of the orientation distribution function of the scattering units in the sample. To represent the scattering profile from a single scatterer, we used Gaussian functions:

$$I(q, \phi') = I_0 \exp\left\{-\frac{(q_3 - q^*)^2}{2b_3^2}\right\} \exp\left\{-\frac{(q_{12})^2}{2b_{12}^2}\right\} \quad (2)$$

DOI: 10.1021/acs.macromol.8b01639
Macromolecules XXXX, XXX, XXX−XXX

where I_0 is the intensity scaling factor, $q_{12} = q \sin(\phi')$, $q_3 = q \cos(\phi')$, q^* is the peak position, b_3 is the radial peak width, and b_{12} is the tangential peak width. To account for the nonuniform orientations of the scattering units in the sample, we used the analytical integration kernel $F(\phi,\phi')$ corresponding to the Onsager orientation distribution.[17,23] Thus, each layer peak required five fitting parameters: radial peak position, radial width, tangential width, degree of orientation, and a scaling factor.

We define our scattering vector $q = 2\pi s$, where s is the scattering vector used by Burger et al.

The amorphous halo in p21AA was fit with a simple Lorentzian function with no angular dependence. For the wide-angle Bragg peak corresponding to the hexagonal chain packing, eq 1 was used, but the tangential width was approximated as a delta function ($b_{12} \rightarrow 0$ in eq 2) with no detriment to the fit quality. A constant background intensity was also added to the fit.

Fitting Algorithm for the First Layer Peak of p21AA at Different Strains. For each scattering pattern that was to be fit, the fitting parameters were adjusted by eye to obtain a reasonably close fit. Then, the following algorithm was employed for at least 200 iterations. The sum of square differences (SSD) was calculated for the current values of the parameters. The SSD was also calculated after increasing *and* decreasing a randomly selected parameter by a predefined step size s, thus obtaining three SSDs corresponding to three parameter values. The parabola defined by the three points was calculated. If the curvature was positive, the parameter value was changed to the minimum of the parabola, or 3s in the direction of the minimum, whichever was smaller. If the curvature was negative, the parameter value was changed by s in the direction of smaller SSD. By repeating this process for 200 iterations, all fitting parameters were optimized to the experimental 2D data.

To assess the repeatability of the fit, for each image, the following procedure was executed five times. All parameter values from the fit above were changed by either $+s^*$, 0, or $-s^*$ (with equal probability), where s^* is a predefined step size that is at least 5 times larger than s. Then the fitting algorithm described above was repeated, again using 200 iterations. The parameter values obtained from the original fit and the five perturbed fits were averaged to obtain the values in Figure 6, and the error bars of Figure 6 represent two standard deviations (95% confidence) based on the distribution of values from the six fits. Finally, we checked that the step size s^* is significantly larger than the confidence interval; if not, the entire procedure was repeated with a larger s^*.

Williamson–Hall Analysis of Size and Disorder. The size and disorder were determined from the layer peak widths using the Williamson–Hall method, which for the Gaussian peak shape assumes

$$\Delta q_{obs} = \Delta q_{instr} + \Delta q_{size} + q_n \Delta q_{disorder} \quad (3)$$

where Δq_{obs} is the observed peak width, Δq_{instr} is the peak width due to instrumental limitations, $2\pi/\Delta q_{size}$ is the crystal size, q_n is the peak position, and $\Delta q_{disorder}$ is a measure of disorder or heterogeneity in the structure. If the disorder is caused by heterogeneous strain, $\Delta q_{disorder}$ is an estimate of the strain inhomogeneity. This analysis assumes that the distance from layer i to layer $i + 1$ does not affect the distance from layer $i + 1$ to layer $i + 2$, which is expected to be the dominant type of disorder in these layered polymer structures. We estimated Δq_{instr} from the peak widths of silver behenate, our calibration standard.

RESULTS

Isotropic Morphologies. The morphology of quiescent, bulk-crystallized p21AA was studied in detail previously.[10,11,14,18,19,24] In summary, p21AA is semicrystalline, with a hairpin chain folding motif within the crystalline regions. The chains fold at the position of each acid group producing alternating layers of carboxylic acids and crystalline alkyl segments, and the center-to-center distance between acid layers is 25 Å. Three peaks with position ratios 1:2:3 corresponding to these layers are visible in the isotropic X-ray scattering (Figure 2). These layered, ordered domains

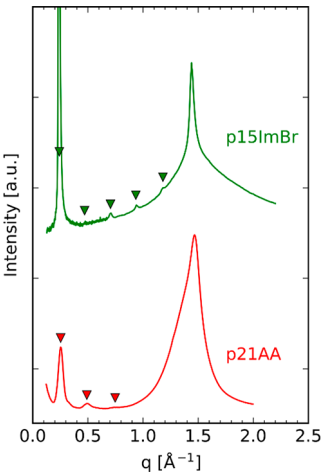

Figure 2. Isotropic (predeformation) X-ray scattering of p15ImBr and p21AA. Triangles indicate the positions of the layer peaks in each material. The high intensity of the first layer peak of p15ImBr arises from the strong electron density contrast between bromine and methylene, while the high sharpness of the peak is related to the structure size and perfection.

coexist with amorphous regions. The alkyl segments pack in a hexagonal fashion, giving rise to a single Bragg reflection at ~1.5 Å^{-1}, which is superimposed on the amorphous halo. The isotropic X-ray scattering of p15ImBr shares some similarities with p21AA (Figure 2)—layers are present at a similar periodicity to p21AA, and there is a single sharp Bragg reflection at ≈1.5 Å^{-1} corresponding to packing of alkyl segments, most likely on a hexagonal lattice.[24]

First, we examine whether p15ImBr exhibits the hairpin chain conformation found in p21AA. The presence of layers could alternatively correspond to a nylon-type structure where the chains are fully extended through the functional group layers within the crystalline regions. However, a nylon-type structure seems unlikely given the large size of the functional group and the very small width of the layer peak, equivalent to the instrumental resolution, indicating a minimum crystal size along the layer normal, ξ_{layer}, of 1300 Å (using the Scherrer equation, $\xi_{layer} \geq 2\pi/\Delta q_{layer}$). The layer periodicity also supports the hairpin chain conformation: in p15ImBr, the periodicity is 26.5 Å, while the all-*trans* length of a monomeric unit is only ≈19 Å. If the structure is similar to p21AA, then the layer periodicity would be ~85% of the monomeric all-*trans* length (minus the carbons in the hairpin fold) plus twice the length of the pendant groups. This estimation yields 27 Å, very close to the experimental value of 26.5 Å. See the Supporting Information for details. It is logical that the bulky, charged imidazolium groups would induce chain folding; they are too large to be incorporated into a polyethylene-like crystal structure, and their charge would likely repel the hydrophobic alkyl segments. Therefore, p15ImBr likely follows a similar set of chain conformations as p21AA within its ordered domains, where the chains execute tight hairpin folds at the position of each functional group. It should be noted that p21ImBr, which has the same functional group periodicity as p21AA, exhibits morphological evolution under tensile deformation similar to p15ImBr,[18] but due to a lack of high quality *in situ* X-ray scattering data for p21ImBr, we present p15ImBr instead.

DOI: 10.1021/acs.macromol.8b01639
Macromolecules XXXX, XXX, XXX–XXX

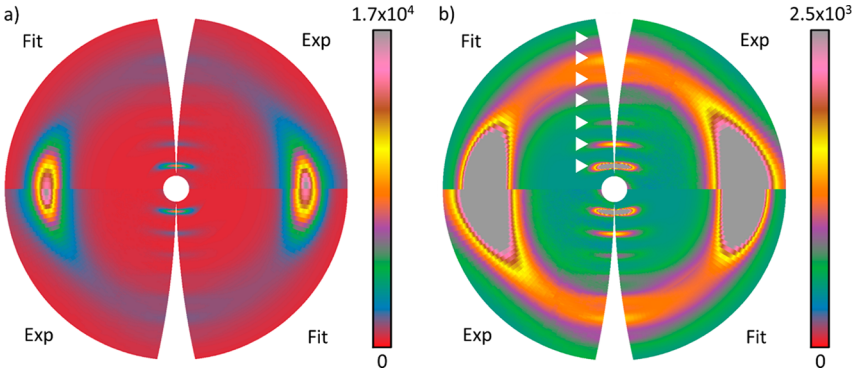

Figure 3. Fraser-corrected[27] 2D X-ray scattering of p21AA at a strain of 500%, with two different intensity scales ((a) 0 to 1.7×10^4 and (b) 0 to 2.5×10^3 arbitrary units). The q range is 0.15−1.9 Å^{-1}. In both (a) and (b), experimental data are shown in the first and third quadrants, and fits are shown in the second and fourth quadrants. Cylindrical symmetry about the fiber axis (vertical axis) is assumed for the fits. The white triangles in (b) indicate the positions of the layer peaks, of which seven harmonics are visible.

A key difference in the predeformation morphologies of p21AA and p15ImBr is the apparent crystal size. p21AA was previously shown to be semicrystalline, with a lamellar crystallite thickness of ∼50−100 Å.[11,14,18,19] Meanwhile, for p15ImBr, there is no evidence of semicrystallinity (see Figure S1). There is no discernible peak at q < 0.2 Å^{-1}, which would correspond to the crystal−amorphous alternations, and the apparent crystal size along the layer normal is unusually large, according to the Scherrer equation. It is therefore likely that p15ImBr is nearly fully crystalline. This situation is similar to that of p21SA, which has sulfonic acid groups pendant to every 21st carbon atom.[1] Single crystals of p21ImBr grown from solution exhibited an unusually large thickness, ≈7000 Å, measured via atomic force microscopy.[24] This is further evidence supporting a very large crystal size (much larger than the chain size) in precise imidazolium bromide polyethylenes.

Water Content. To quantify the amount of water in each polymer at ambient conditions (∼21 °C and ∼40% relative humidity), TGA was performed, and the thermograms are shown in Figure S2 and summarized in Table 1. p15ImBr contains 3.5 wt % of water, nearly 1 mol of water per mole of imidazolium, which is significantly more water than p21AA (0.7 wt %). In nylon-6, the yield stress with 3.3 wt % water was reduced by about 20−40% compared with <0.1 wt % water,[25] so the water content of p15ImBr could have an appreciable effect on its yield stress. However, the presence of water did not reduce strain hardening in nylon-6 (in fact, it increased strain hardening),[26] so the lack of strain hardening in p15ImBr is likely not caused by the water content. In both p21AA and p15ImBr, the water is likely to associate with the functional groups rather than the alkyl segments due to the hydrophobicity of the alkyl segments.

Morphology at High Strain. X-ray scattering was collected during tensile deformation. In p21AA, the layer peaks during deformation quickly become non-arc-like and instead were in between arcs (constant q_{max} over azimuthal angle) and flat lines. Therefore, both the radial and tangential components of the peak shape from a single structural unit must be considered along with the nonuniform orientation of structural units. To obtain useful information from these peculiarly shaped peaks at a strain of 500%, we performed a full quantitative fit of the scattering pattern using the equations presented by Burger et al.[17] (Figure 3). The intensity scale for the experiment and the fit in Figure 3a highlights the equatorial peak and first layer peak, while that in Figure 3b highlights the higher order layer peaks.

The Bragg reflection at ≈1.5 Å^{-1} with preferential orientation toward the equator was fit with a Gaussian function in the radial direction, weighted by an Onsager distribution[23] to capture the imperfect orientation. The tangential peak width could be ignored, i.e., represented by a delta function. Note that this reflection had a narrower head and longer tail than the Gaussian function that was used to fit it (Figure 3). This unusual peak shape may be related to an anisotropic amorphous halo and a dispersity in crystal sizes along the 100_{hex} vector. The fit was not improved by using a Lorentzian or a pseudo-Voigt profile instead of Gaussian, nor was it improved by including a finite tangential peak width. Still, the 2D peak shape was mostly captured by the fit.

Each meridional layer peak of p21AA was modeled with a 2D Gaussian function, and an Onsager orientation distribution was used to model the imperfect orientation of these peaks. By this method we obtain an excellent fit at a strain of 500% (Figure 3). Fitting the meridional peaks yields a tangential peak width of ≈0.3 Å^{-1}, indicating that the layered structure has a size perpendicular to the layer normal of ≈20 Å. Meanwhile, the radial peak width was an order of magnitude smaller, indicating elongated, nanofibril-like layered structures, wherein the layer normal is parallel to the long dimension of the structure. The equatorial orientation of the wide-angle Bragg reflection indicates that the 100_{hex} vector is perpendicular to the layer normal. The orientation of the equatorial peak is poorer than that of the meridional peaks, likely indicating considerably more disorder in the registry of the chains than in the acid layers.

The radial widths of the layer peaks extracted from the 2D fits to p21AA at strain = 500% are plotted in Figure 4 along with the radial peak widths of the isotropic sample. These radial widths were analyzed according to the Williamson−Hall method (see Methods section for details), which decouples the peak broadening due to size from the broadening due to disorder and heterogeneity. For isotropic p21AA, only two peak widths can be accurately measured, so fitting a line is suspect, especially because the intensity of the second peak is quite low. However, at high strain, a line is well fit to the data and the y-intercept is effectively zero, indicating a very large (at least 570 Å or more than 22 layers) correlation length normal to the layers. The equivalent heterogeneity in layer period (25 Å) to cause the observed slope in Figure 4 would be 0.6%

DOI: 10.1021/acs.macromol.8b01639
Macromolecules XXXX, XXX, XXX−XXX

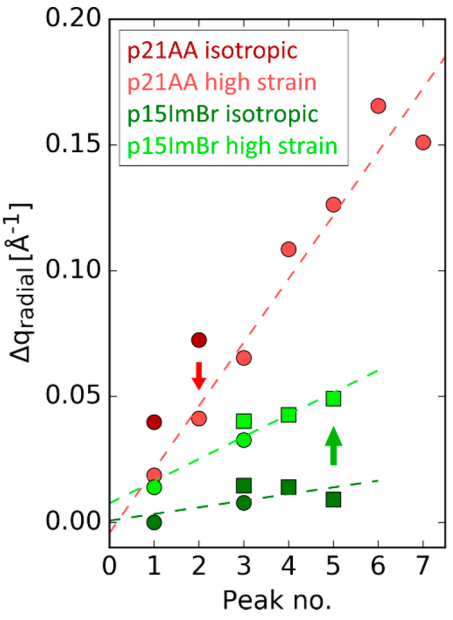

Figure 4. Layer peak radial width as a function of the peak number for p21AA, in the isotropic (predeformation) state and at a strain of 500%, and p15ImBr, in the isotropic state and at a strain of 300%. The squares signify simultaneous data collection on a second detector with a different instrumental resolution. According to the Williamson–Hall method, linear fits provide estimates of the structure size (y-intercept) and degree of disorder (slope), assuming disorder of the first kind. The instrumental resolution has been subtracted.

(≈0.15 Å). The ordering and/or the size clearly increases relative to the isotropic case.

The opposite trend is observed for p15ImBr (Figure 4), wherein the layer peaks were fit in 1D (I vs q) with simple Lorentzian profiles. Before deformation, p15ImBr exhibits an exceptionally small radial layer peak width, essentially equivalent to the instrumental resolution, indicating a structure size of at least 1300 Å along the layer normal (at least 50 layers) and minimal disorder. Upon deformation, the disorder increases by at least a factor of 3 but remains quite low—assuming heterogeneity in the layer period is the cause of the disorder, this heterogeneity is calculated to be only 0.2% (≈0.05 Å). This is 3 times lower than that of p21AA at high strain. In p15ImBr, the degree of azimuthal orientation of the layer peak is quite high, but the degree of orientation of the Bragg reflection at ≈1.5 Å^{-1} appears less so (Figure 1d). Note that this does not necessarily indicate a difference in orientation distribution of these two structural features; it is merely a consequence of the perpendicular orientation.[17]

Morphological Evolution during Deformation. To track the morphology during deformation in p21AA, the first layer peak was fit in 2D at strains from 0 to 500%, and example 2D fits at four strains are presented in Figure 5. The fitting results are plotted in Figure 6b–e along with the engineering stress–strain behavior, Figure 6a. The overall trend is a large initial change at yield (strain ∼50%), followed by gradual or minimal changes after yield. The layer period (d^*) increases by about 1 Å, or 4%, upon yielding, and is essentially constant thereafter. This rapid increase in layer period may be indicative of chain stretching via a reduction of the number of gauche conformations but cannot be due to simple stretching of all-*trans* chains: the expected change in length of an all-*trans* polyethylene chain is only 0.005% at the stresses applied here.[28] The change in layer period could also be due to a more profound structural change. Indeed, the structure size perpendicular to the layer normal, ξ_{perp}, undergoes a dramatic change upon yield, decreasing from at least 70 Å to ≈20 Å (Figure 6d). This indicates strain-induced fragmentation of the crystallites into elongated, narrow fibrils. Based on the 100_{hex} d-spacing of 4.39 Å, these fibrils are only 4–5 chains wide. A cross section of a cylindrical fibril therefore contains ∼15–20 stems. The radial width of the 100_{hex} peak after yield corroborates this fibril size, indicating an apparent size of 24 Å. The dramatic decrease in intensity of the SAXS peak indicates a loss of the crystalline–amorphous alternation (Figure S1a). This is a significant structural change from the isotropic, quiescent morphology.

In p21AA, the apparent structure size along the layer normal increases by a factor of 2 during deformation (Figure 6c). However, as seen in Figure 4, a large component of the radial peak width is caused by disorder, so this increase of apparent size during deformation may be interpreted as increasing ordering. The Hermans orientation parameter[29] (HOP) increases significantly upon yield and then continues to

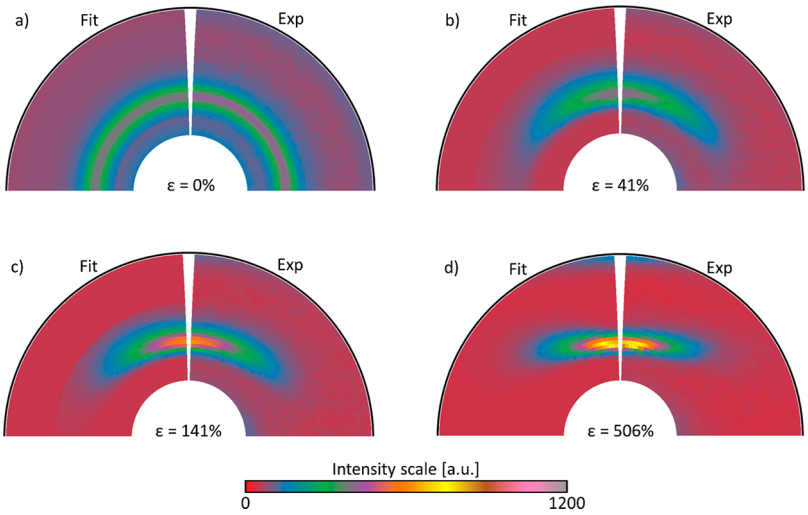

Figure 5. Fits of the first layer peak of p21AA at four strains: (a) 0%, (b) 41%, (c) 141%, and (d) 506%. The q range shown is 0.15–0.49 Å^{-1}.

DOI: 10.1021/acs.macromol.8b01639
Macromolecules XXXX, XXX, XXX–XXX

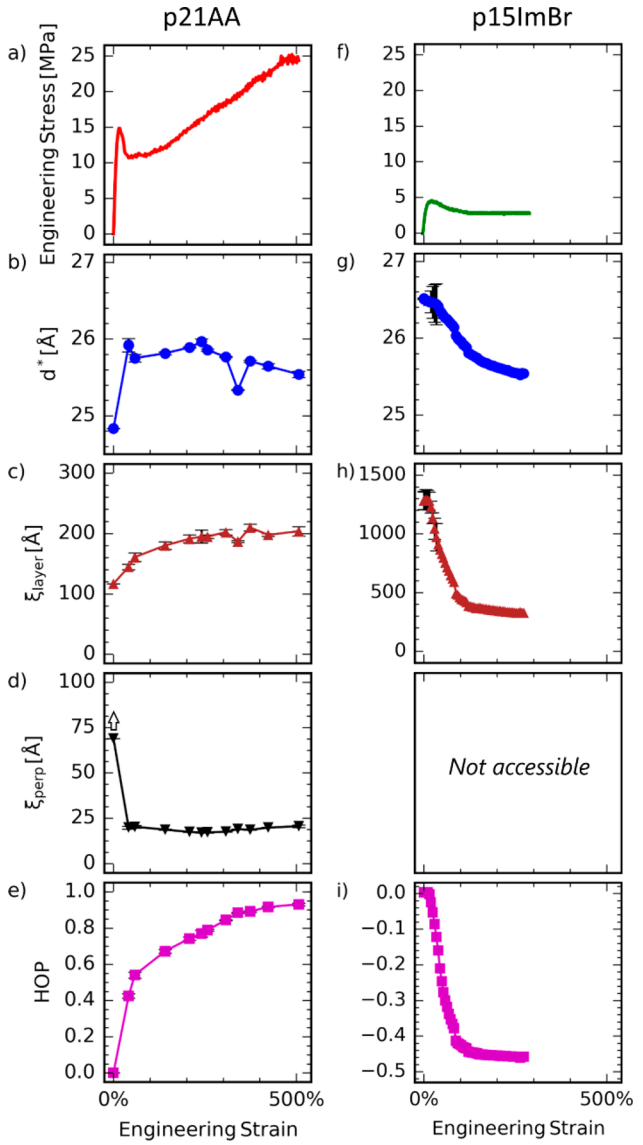

Figure 6. (a, f) Engineering stress−strain curves for p21AA and p15ImBr. (b−e) Results of 2D fitting of the first layer peak of p21AA. (g−i) Results of 1D fitting of the first layer peak of p15ImBr as a function of engineering strain. (b, g) Layer period, obtained from peak position. (c, h) Apparent structure size along layer normal, obtained from the radial peak width. (d) Apparent structure size perpendicular to layer normal, obtained from peak width in tangential direction. (e, i) Hermans orientation parameter. The error bars for p21AA represent 95% confidence based on repeatability of the 2D fit. The error bars for p15ImBr represent 95% confidence based on the variation of the 1D fits at different azimuthal angles at a given strain. ξ_{perp} is not accessible for p15ImBr because the peak shape follows a circular arc, so the tangential peak width is indistinguishable from a delta function.

increase steadily (Figure 6e). Thus, the deformation *after* yield is largely accomplished not by major changes to the structural units, but by increasing orientation of those units as molecules are transported along the tensile axis. Note that necking was observed in both p21AA and p15ImBr, so the strain experienced by the region of the sample probed by the X-ray beam is not the engineering strain.

p15ImBr exhibits largely opposite trends to p21AA during deformation (Figure 6f−i). As shown in Figure 1d, the layers of p15ImBr orient with the layer normal toward the equator during deformation, and this is reflected in the HOP approaching −0.5 in Figure 6i. The layer period in p15ImBr decreases during deformation, in contrast with p21AA. This is likely the result of the perpendicular orientation; applying stress perpendicular to the layer normal would tend to elongate the structure along the fiber axis and therefore compress the structure along the layer normal assuming Poisson's ratio is positive. The fact that d^* continues to decrease at high strains could be due to increasing *true* stress as the sample thins, even though the engineering stress is constant (Figure 6f). The decrease of d^* could also be associated with increasing tilting of the crystalline stems relative to the layer normal during deformation.

DISCUSSION

The key structural difference between p21AA and p15ImBr during deformation is the breaking up of crystallites in p21AA. This occurs near the yield point—the nanofibrillization occurs between 0 and 50% strain, after which the structure size perpendicular to the layer normal is ≈20 Å in p21AA (Figure 6d). This lateral size is confirmed by the 100_{hex} peak width. These nanofibrils are very elongated, having a length beyond detection according to the Williamson−Hall analysis shown in Figure 4. Order along the layer normal is improved after deformation, as seen by the reduced layer peak radial width. Deformation beyond the yield point involves increasing the degree of orientation of the fibrils toward the tensile axis; aside from this, the changes to the structural units are minimal after yield in p21AA. This suggests that the deformation mechanism after yield involves the nanofibrils sliding past one another as they orient along the tensile axis, similar to what has been proposed in polyethylene.[30,31] However, polyethylene contains much wider fibrils, on the order of 1 μm in diameter.[32] The relative orientation of the acid layer peak and the 100_{hex} equatorial peak at high deformation is also intriguing because they are essentially perpendicular (see Figure 3). According to our previous atomistic simulations on large crystals in the absence of strain,[10] the layer normal cannot be coaxial with the chain in large crystals because of packing constraints; in the simulations, it is tilted by 32°. However, for narrow fibrils only 4−5 chains in diameter, this packing issue may not be significant because the fibril can be somewhat wider near the acid layers.

In p15ImBr, the crystals remain largely intact, although their disorder increases with deformation (Figure 4). Why do these crystals remain largely intact while those in p21AA fragment into nanofibrils? There are likely many contributing factors. The predeformation morphology may play a role. Before deformation, p15ImBr appears to be nearly fully crystalline; the layer peak indicates a very large crystal size, and there is no SAXS peak that would signify crystalline−amorphous alternation (Figure S1). Without amorphous regions, onset of crystal fragmentation may be less likely. Another factor is the charged functional groups. The positive imidazolium groups together with negative bromide ions within a layer likely provide greater cohesive stability and resistance to fragmentation compared with the hydrogen-bonding carboxylic acid groups, whose interactions are shorter range. At the same time, the low yield stress of p15ImBr suggests that the deformation of its layered structure is relatively facile, perhaps owing to weaker ionic interactions relative to H-bonding of the carboxyl groups. The imidazolium bromide groups may also exhibit a stronger repulsion toward the hydrophobic alkyl segments,

DOI: 10.1021/acs.macromol.8b01639
Macromolecules XXXX, XXX, XXX−XXX

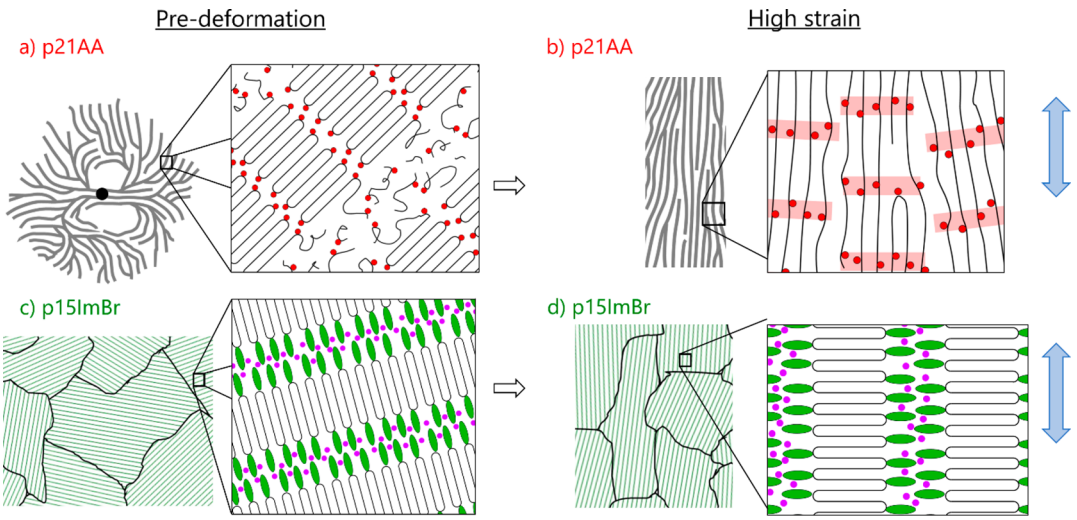

Figure 7. Schematic of the morphologies of p21AA (a, b) and p15ImBr (c, d) before deformation and at high tensile strain. In (a) and (c), the orientations of the structural features are isotropic throughout the sample, while in (b) and (d), the schematics represent preferred orientation throughout the sample. In (a) and (b), the red circles represent carboxylic acid groups, and in (c) and (d), the green ovals represent imidazolium side groups and the magenta circles represent bromide ions. Water molecules are not shown.

preventing the layers from breaking apart. A related factor is the higher melting point of p15ImBr (70 °C) compared with p21AA (46 °C); in polyolefins, chains are known to be more mobile close to their melting point,[33] which could facilitate fragmentation in p21AA more than in p15ImBr. Finally, the water present in the p15ImBr sample could facilitate some degree of slippage between layers, permitting plastic deformation without nanofibrillization of the crystals.

Figure 7 illustrates our conclusions about the morphological evolution of p21AA and p15ImBr under uniaxial tensile deformation. Before deformation, both polymers exhibit hairpin chain folding at the positions of the functional groups. Initially, p21AA is semicrystalline with a spherulitic mesostructure[11] (Figure 7a). At high strain, the morphology becomes dominated by elongated fibril-like structures with widths of ≈20 Å, which are oriented along the tensile axis (Figure 7b). Meanwhile, p15ImBr initially has high crystallinity with randomly oriented domains (Figure 7c). At high strains, the domains orient with the ionic layer normal vectors perpendicular to the tensile axis, and the degree of disorder increases and/or the domain size decreases (Figure 7d).

The reason for the perpendicular orientation of the chains in p15ImBr (Figure 1d) appears to be related to the preservation of the local crystal structure. Given the hairpin chain folding motif expected in p15ImBr,[10] the net chain direction is actually orthogonal to the layer normal, not parallel. Because covalent bonds are the least subject to breaking, it is logical that the chain end-to-end vector will orient along the tensile axis. In fact, this orientation (layer normal vectors aligning perpendicular to the tensile axis) is seen in the preyield stages of tensile deformation in p21AA, as we reported previously,[11] before the crystallites fragment.

CONCLUSION

In situ X-ray scattering during tensile deformation of two precisely periodic functional polyethylenes is reported along with quantitative 2D fitting of the X-ray scattering patterns. One polyethylene contains pendant carboxylic acid groups every 21st carbon (p21AA), and one contains pendant imidazolium bromide groups every 15th carbon (p15ImBr). We find strikingly different behaviors of the two polymers during deformation. In p21AA, which begins as semicrystalline, the crystallites fragment upon yielding and a nanofibrillar morphology ensues, with fibril diameter ∼20 Å. The nanofibrils contain layers of acid groups and orient progressively toward the tensile axis during postyield deformation. In p15ImBr, which appears to begin as nearly fully crystalline, the chain-folding motif is mostly intact after deformation, with some increase in disorder. In p15ImBr, the layers orient with their normal vectors *perpendicular* to the tensile axis, in contrast with p21AA. Given the chain-folding motif, this perpendicular orientation causes the chain end-to-end vectors to be oriented along the tensile axis. The result of these morphological differences is a pronounced postyield strain hardening in p21AA and minimal strain hardening in p15ImBr. This suggests that the fragmentation of the crystallites and fibrillization in p21AA plays an important role in the strain-hardening mechanism. This study also highlights the powerful tunability of precise polymers; changing the functional group from a hydrogen-bonding moiety to a charged moiety has a dramatic impact on both morphology and mechanical response during tensile deformation.

ASSOCIATED CONTENT

Supporting Information

The Supporting Information is available free of charge on the ACS Publications website at DOI: 10.1021/acs.macromol.8b01639.

Discussion of the hairpin folding motif in p15ImBr; *in situ* SAXS during tensile deformation; and TGA thermograms (PDF)

AUTHOR INFORMATION

Corresponding Author

*E-mail: winey@seas.upenn.edu (K.I.W.).

ORCID

Edward B. Trigg: 0000-0002-4723-650X

Karen I. Winey: 0000-0001-5856-3410

DOI: 10.1021/acs.macromol.8b01639
Macromolecules XXXX, XXX, XXX−XXX

Present Addresses

E.B.T.: Air Force Research Laboratory RXCC, Wright-Patterson Air Force Base, Dayton, OH 45433-7750.
L.R.M.: Exponent, 3440 Market St. #600, Philadelphia, PA 19104.

Notes

The authors declare no competing financial interest.

■ ACKNOWLEDGMENTS

We acknowledge funding from the National Science Foundation (NSF) DMR 1506726 and NSF PIRE 1545884. We also acknowledge the Laboratory for Research on the Structure of Matter (LRSM), supported by NSF DMR 17-20530. A portion of this work was performed at the DuPont−Northwestern−Dow Collaborative Access Team (DND-CAT) located at Sector 5 of the Advanced Photon Source (APS). DND-CAT is supported by E.I. DuPont de Nemours & Co., The Dow Chemical Company, and Northwestern University. Use of the APS, an Office of Science User Facility operated for the U.S. Department of Energy (DOE) Office of Science by Argonne National Laboratory, was supported by the U.S. DOE under Contract DE-AC02-06CH11357. We express our gratitude to Steve Weigand (DuPont) and William E. Guise (DuPont) for experimental work and beamline setup at the APS. We acknowledge Prof. Kenneth B. Wagener and his research group, who previously supplied p21AA and p15ImBr for our joint publications.[14,16,18−20,34] We are grateful to Paul A. Heiney (University of Pennsylvania) and Yimin Mao (National Institute of Standards and Technology) for fruitful discussions.

■ REFERENCES

(1) Trigg, E. B.; Gaines, T. W.; Maréchal, M.; Moed, D. E.; Rannou, P.; Wagener, K. B.; Stevens, M. J.; Winey, K. I. Self-Assembled Highly Ordered Acid Layers in Precisely Sulfonated Polyethylene Produce Efficient Proton Transport. *Nat. Mater.* **2018**, *17*, 725−731.
(2) Rosales, A. M.; Segalman, R. A.; Zuckermann, R. N. Polypeptoids: A Model System to Study the Effect of Monomer Sequence on Polymer Properties and Self-Assembly. *Soft Matter* **2013**, *9* (35), 8400−8414.
(3) Hosoda, S.; Nozue, Y.; Kawashima, Y.; Utsumi, S.; Nagamatsu, T.; Wagener, K.; Berda, E. B.; Rojas, G.; Baughman, T. W.; Leonard, J. K. Perfectly Controlled Lamella Thickness and Thickness Distribution: A Morphological Study on ADMET Polyolefins. *Macromol. Symp.* **2009**, *282* (1), 50−64.
(4) Schulz, M. D.; Wagener, K. B. Precision Polymers through ADMET Polymerization. *Macromol. Chem. Phys.* **2014**, *215*, 1936−1945.
(5) Seitz, M. E.; Chan, C. D.; Opper, K. L.; Baughman, T. W.; Wagener, K. B.; Winey, K. I. Nanoscale Morphology in Precisely Sequenced Poly(Ethylene-Co-Acrylic Acid) Zinc Ionomers. *J. Am. Chem. Soc.* **2010**, *132* (23), 8165−8174.
(6) Bolintineanu, D. S.; Stevens, M. J.; Frischknecht, A. L. Atomistic Simulations Predict a Surprising Variety of Morphologies in Precise Ionomers. *ACS Macro Lett.* **2013**, *2* (3), 206−210.
(7) Ortmann, P.; Trzaskowski, J.; Krumova, M.; Mecking, S. Precise Microstructure Self-Stabilized Polymer Nanocrystals. *ACS Macro Lett.* **2013**, *2* (2), 125−127.
(8) Sampath, J.; Hall, L. M. Impact of Ionic Aggregate Structure on Ionomer Mechanical Properties from Coarse-Grained Molecular Dynamics Simulations. *J. Chem. Phys.* **2017**, *147* (13), 134901.
(9) Sampath, J.; Hall, L. M. Impact of Ion Content and Electric Field on Mechanical Properties of Coarse-Grained Ionomers. *J. Chem. Phys.* **2018**, *149* (16), 163313.
(10) Trigg, E. B.; Stevens, M. J.; Winey, K. I. Chain Folding Produces a Multilayered Morphology in a Precise Polymer: Simulations and Experiments. *J. Am. Chem. Soc.* **2017**, *139* (10), 3747−3755.
(11) Trigg, E. B.; Middleton, L. R.; Moed, D. E.; Winey, K. I. Transverse Orientation of Acid Layers in the Crystallites of a Precise Polymer. *Macromolecules* **2017**, *50* (22), 8988−8995.
(12) Mandal, J.; Krishna Prasad, S.; Rao, D. S. S.; Ramakrishnan, S. Periodically Clickable Polyesters: Study of Intrachain Self-Segregation Induced Folding, Crystallization, and Mesophase Formation. *J. Am. Chem. Soc.* **2014**, *136* (6), 2538−2545.
(13) Roy, R. K.; Gowd, E. B.; Ramakrishnan, S. Periodically Grafted Amphiphilic Copolymers: Nonionic Analogues of Ionenes. *Macromolecules* **2012**, *45* (7), 3063−3069.
(14) Middleton, L. R.; Szewczyk, S.; Azoulay, J.; Murtagh, D.; Rojas, G.; Wagener, K. B.; Cordaro, J.; Winey, K. I. Hierarchical Acrylic Acid Aggregate Morphologies Produce Strain-Hardening in Precise Polyethylene-Based Copolymers. *Macromolecules* **2015**, *48* (11), 3713−3724.
(15) Middleton, L. R.; Trigg, E. B.; Yan, L.; Winey, K. I. Deformation-Induced Morphology Evolution of Precise Polyethylene Ionomers. *Polymer* **2018**, *144*, 184−191.
(16) Middleton, L. R.; Trigg, E. B.; Schwartz, E.; Opper, K. L.; Baughman, T. W.; Wagener, K. B.; Winey, K. I. Role of Periodicity and Acid Chemistry on the Morphological Evolution and Strength in Precise Polyethylenes. *Macromolecules* **2016**, *49* (21), 8209−8218.
(17) Burger, C.; Hsiao, B. S.; Chu, B. Preferred Orientation in Polymer Fiber Scattering. *Polym. Rev.* **2010**, *50* (1), 91−111.
(18) Buitrago, C. F.; Jenkins, J. E.; Opper, K. L.; Aitken, B. S.; Wagener, K. B.; Alam, T. M.; Winey, K. I. Room Temperature Morphologies of Precise Acid- and Ion-Containing Polyethylenes. *Macromolecules* **2013**, *46* (22), 9003−9012.
(19) Baughman, T. W.; Chan, C. D.; Winey, K.; Wagener, K. B. Synthesis and Morphology of Well-Defined Poly (Ethylene-Co-Acrylic Acid) Copolymers. *Macromolecules* **2007**, *40* (18), 6564−6571.
(20) Aitken, B. S.; Buitrago, C. F.; Heffley, J. D.; Lee, M.; Gibson, H. W.; Winey, K. I.; Wagener, K. B. Precision Ionomers: Synthesis and Thermal/Mechanical Characterization. *Macromolecules* **2012**, *45* (2), 681−687.
(21) Trigg, E. B. FiberByPy. GitHub Repository; https://github.com/etrigg/FiberByPy, 2017.
(22) Burger, C.; Zhou, H. W.; Sičš, I.; Hsiao, B. S.; Chu, B.; Graham, L.; Glimcher, M. J. Small-Angle X-Ray Scattering Study of Intramuscular Fish Bone: Collagen Fibril Superstructure Determined from Equidistant Meridional Reflections. *J. Appl. Crystallogr.* **2008**, *41* (2), 252−261.
(23) Onsager, L. The Effects of Shape on the Interation of Colloidal Particles. *Ann. N. Y. Acad. Sci.* **1949**, *51*, 627−659.
(24) Yan, L.; Bustillo, K. C.; Panova, O.; Minor, A. M.; Winey, K. I. Solution-Grown Crystals of Precise Acid- and Ion-Containing Polyethylenes. *Polymer* **2018**, *135*, 111−119.
(25) Galeski, A.; Argon, A. S.; Cohen, R. E. Changes in the Morphology of Bulk Spherulitic Nylon 6 Due to Plastic Deformation. *Macromolecules* **1988**, *21* (9), 2761−2770.
(26) Miri, V.; Persyn, O.; Lefebvre, J. M.; Seguela, R. Effect of Water Absorption on the Plastic Deformation Behavior of Nylon 6. *Eur. Polym. J.* **2009**, *45* (3), 757−762.
(27) Fraser, R. D. B.; Macrae, T. P.; Miller, A.; Rowlands, R. J. Digital Processing of Fibre Diffraction Patterns. *J. Appl. Crystallogr.* **1976**, *9*, 81−94.
(28) Treloar, L. R. G. Calculations of Elastic Moduli of Polymer Crystals: 1. Polyethlene and Nylon 66. *Polymer* **1960**, *1*, 95−103.
(29) Hermans, J. J.; Hermans, P. H.; Vermaas, D.; Weidinger, A. Quantitative Evaluation of Orientation in Cellulose Fibres from the X-Ray Fiber Diagram. *Recl. des Trav. Chim. des Pays-Bas* **1946**, *65* (6), 427−447.
(30) Hiss, R.; Hobeika, S.; Lynn, C.; Strobl, G. Network Stretching, Slip Processes, and Fragmentation of Crystallites during Uniaxial

DOI: 10.1021/acs.macromol.8b01639
Macromolecules XXXX, XXX, XXX−XXX

Drawing of Polyethylene and Related Copolymers. A Comparative Study. *Macromolecules* **1999**, *32* (13), 4390−4403.
(31) Peterlin, A. Molecular Model of Drawing Polyethylene and Polypropylene. *J. Mater. Sci.* **1971**, *6* (6), 490−508.
(32) Drummond, K. M.; Shanks, R. A.; Cser, F. Morphological Analysis of Linear Low Density Polyethylene Films by Atomic Force Microscopy. *J. Appl. Polym. Sci.* **2002**, *83* (4), 777−784.
(33) Mao, Y.; Li, X.; Burger, C.; Hsiao, B. S.; Tsou, A. H. 2D WAXS/SAXS Study on Isotactic Propylene-1-Butylene Random Copolymer Subjected to Uniaxial Stretching: The Influence of Temperature. *Polymer* **2013**, *54* (4), 1432−1439.
(34) Choi, U. H.; Middleton, L. R.; Soccio, M.; Buitrago, C. F.; Aitken, B. S.; Masser, H.; Wagener, K. B.; Winey, K. I.; Runt, J. Dynamics of Precise Ethylene Ionomers Containing Ionic Liquid Functionality. *Macromolecules* **2015**, *48*, 410−420.

DOI: 10.1021/acs.macromol.8b01639
Macromolecules XXXX, XXX, XXX−XXX